

Eur. Phys. J. E (2014) 37: 39

DOI 10.1140/epje/i2014-14039-8

Elapsed time for crack formation during drying

F. Giorgiutti-Dauphiné and L. Pauchard

Elapsed time for crack formation during drying

F. Giorgiutti-Dauphiné and L. Pauchard^a

Univ Paris-Sud, CNRS, F-91405, Lab FAST, Bat 502, Campus Univ, Orsay, F-91405, France

Received 23 January 2014 and Received in final form 18 April 2014

Published online: 26 May 2014 – © EDP Sciences / Società Italiana di Fisica / Springer-Verlag 2014

Abstract. The drying of colloidal films usually leads to mechanical instabilities that affect the uniformity of the final deposit. The resulting patterns are the signature of the mechanical stress, and reveal the way the system consolidates. We report experimental results on the crack patterns induced by the drying of sessile drops of concentrated dispersions. Crack patterns exhibit a well-defined spatial order, and a regular temporal periodicity. In addition, the onset of cracking occurs after a well-defined elapsed time that depends on the mechanical properties of the gel, and on the drying kinetics. The estimation of the time elapsed before cracks form is related to the elastic properties of the material. This is supported by quantitative measurements using indentation testing and by a simple scaling law derived from poro-elastic theory.

1 Introduction

Most coatings are made by depositing a volatile liquid that contains dispersed colloidal particles. The liquid is then evaporated until a dry film is obtained. High mechanical stresses usually give rise to major defects such as cracks or debonding [1–3]. In practice, the control of these phenomena is crucial for all the coating technologies since they significantly alter the final film quality, and consequently need to be avoided. However, such defects are characteristic of the mechanical properties of the material and the conditions of consolidation. In that way, crack pattern can be useful in Art field where craquelures provide informations on the materials (pigments) or the painting techniques used by the artists [4]. In addition recent interest has emerged in interpreting solute patterns of evaporated biological fluid droplets for medical screening and diagnostic purposes [5] or in forensic [6].

In this article, a series of experimental work supported by poro-elasticity modeling report the occurrence of crack formation induced by the drying process of concentrated silica dispersions. The experiments are carried out in the geometry of an isolated drop deposited onto a flat and non-porous surface. Despite of the complexity of this geometry related to the existence of a three-phase line and the thickness gradient, reproducible experiments in directional propagation of cracks are permitted. In particular, crack patterns exhibit regular spatial, and temporal periodicity. The cracking onset occurs after a clearly defined elapsed time, that depends on both the silica material, and the drying kinetics. As a result the elastic modulus of the gel phase at onset of cracking can be determined, and compared with measurements using indentation testing.

2 Methods

Experiments are performed with concentrated aqueous dispersions of charged silica particles Ludox SM-30, HS-40, and TM-50 commercially available from Sigma-Aldrich. The main properties of the dispersions are reported in table 1. The polydispersity index is of the order of 0.15. The pH is about 9, so the particle surface bears a high negative charge density. In the absence of evaporation, the stability of an aqueous colloidal dispersion is governed by the interparticle colloidal interaction, *i.e.*, by the competition between van der Waals attraction and electrostatic repulsion [7,8]. During evaporation, colloidal particles aggregate until a irreversible solidification of particles into a rigid connected network is formed. The gelation process is well described in terms of percolation theory [9].

In the following SM-30 is used without treatments, while HS-40, and TM-50 are diluted using pure water (milliQ quality, resistivity: 18 MΩ cm) at pH = 9.5 by addition of NaOH. A weight ratio of 90/10 (HS-40/water) and 75/25 (TM-50/water) are chosen to obtain similar initial volume fraction $\phi_0 = 0.20$.

The desiccation geometry used in the experiments is that of a drop, with a radius R_0 , deposited on carefully cleaned microscope glass slides. Before use the substrates are carefully cleaned with ethanol, then kept dehydrating in an oven at 100 °C. This thermal treatment, in particular the duration spent at high temperature (ranging between a few minutes and a few days), allows us to vary the contact angle in a wide range, from $\theta_0 = 10^\circ$ to 50° . Under the condition $2R_0 < \kappa^{-1} = \sqrt{\gamma_{w,a}/\rho g} \sim 3$ mm, that is the water/air surface tension $\gamma_{w,a}$ dominates the gravity, the initial sessile drop is a spherical cap shape (side view in fig. 1a).

^a e-mail: pauchard@fast.u-psud.fr

Table 1. Main properties of silica dispersions used in this paper. The particle diameter is noted $2a$ (from ref. [10] (p. 324)). E_p^{ind} : elastic moduli of different silica gels (measurements using indentation testing at time t_f). E_p : elastic moduli deduced from eq. (5). Drying conditions: $RH \sim 50\%$ at room temperature.

| Silica dispersion | $2a$ (nm) | ϕ_0 | ρ (kg m^{-3}) | E_p^{ind} ($\pm 0.3 \text{ GPa}$) | E_p ($\pm 0.4 \text{ GPa}$) |
|-------------------|-----------|----------|-------------------------------|--|---------------------------------|
| SM-30 | 10 | 0.15 | 1180 | 3.2 | 3.75 |
| HS-40 | 16 | 0.20 | 1250 | 2.5 | 2.85 |
| TM-50 | 26 | 0.20 | 1260 | 2.0 | 2.25 |

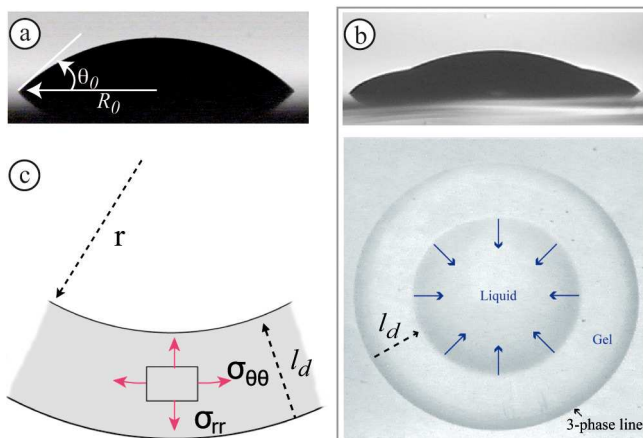


Fig. 1. (a) Image in side view just after the colloidal drop deposition on a glass microscope slide (initial volume fraction is $\phi_0 = 0.20$; initial contact angle $\theta_0 = 30^\circ$, and drop base diameter $2R_0 = 3 \text{ mm}$). (b) Side and top view of the sessile drop taken 15 min after deposition (HS-40 dispersion, drying conditions are $T = 20^\circ$, $RH = 50\%$). A solid gelled foot builds up near the three-phase line, while the central part is fluid and shrinks. (c) Radial σ_{rr} and ortho-radial $\sigma_{\theta\theta}$ components of the stress field in a part of the solid foot at the drop periphery in cylindrical coordinates.

The setup is placed inside a chamber with a relative humidity RH controlled by a variable flow of nitrogen bubbling in a water bath. The flow is stopped before the beginning of the experiment to prevent any convection inside the chamber. In particular, low relative humidity, $RH = 20 \pm 2\%$, is controlled using a saturated salt solution (potassium acetate) at room temperature.

Drop profiles and crack patterns formation are investigated using video recordings and image analysis. Side views are mainly used to measure the contact angle of the drop deposited on the substrate: the contact angle is found to be constant in a given experiment.

The elastic moduli E_p of gelled films are measured using indentation testing (CSM Instruments Micro Indentation Tester) with a spherical indenter [11]. The indenter, initially in contact with the surface of the gel, is driven in the material until a maximal load $F_{\max} = 100 \text{ mN}$ with a loading speed 100 mN/min . The maximal force is held during 30 s. Then, the load is decreased until zero with

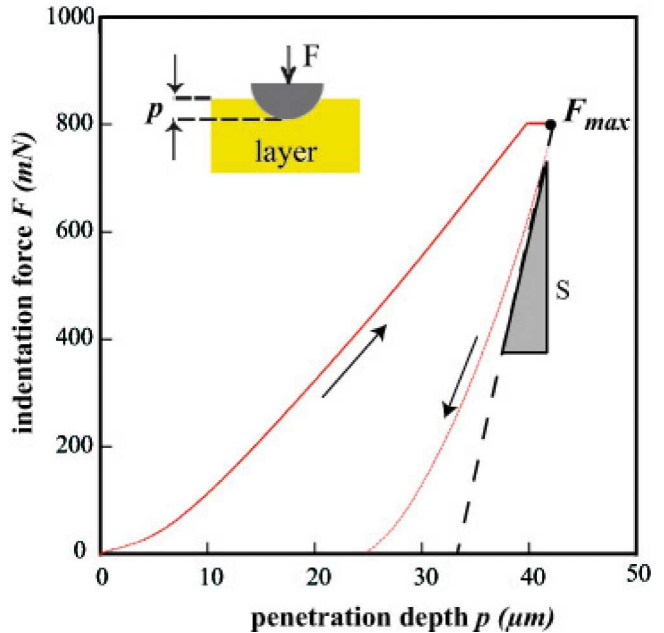


Fig. 2. Typical load-displacement curve resulting in the indentation force F as a function of the penetration depth p .

the same speed. The standard way to estimate the elastic modulus from the indentation load-displacement curve uses the initial slope S of the unloading curve (fig. 2). Measurements are performed on a thick film in the absence of de-adhesion film/substrate. The film thickness is at least 10 times larger than the maximum value of the penetration depth of the indenter: in this way the measurements are not influenced by the substrate. The elastic modulus measured using indentation testing will be noted E_p^{ind} in the following.

3 Results

3.1 Drying a sessile drop of a concentrated colloidal dispersion

In our experimental situations, evaporation is limited by diffusion of water into air. Contrasting with the case of a pure water drop that recedes with a constant contact angle, a drop of a concentrated colloidal dispersion recedes with a constant contact base. Thus, as long as it is the dominant mechanism, the evaporation rate V_E of a sessile drop expresses as [12]:

$$V_E = \frac{D_w}{R_0} \frac{n_{wsat}}{n_1} A(\theta_0)(1 - RH), \quad (1)$$

where n_{wsat} is the water concentration in the vapor at the air-water interface, and n_1 is the number of moles per unit volume in liquid water; $A(\theta_0)$ is a numerical factor related to the shape of the isoconcentration curves of water in air [13] (typically $A(\theta_0)$ varies from 1.3 to 1 when θ_0 increases from 20° to 90°); D_w is the diffusion coefficient of water into air (typically $D_w = 25 \times 10^{-6} \text{ m}^2/\text{s}$ at room

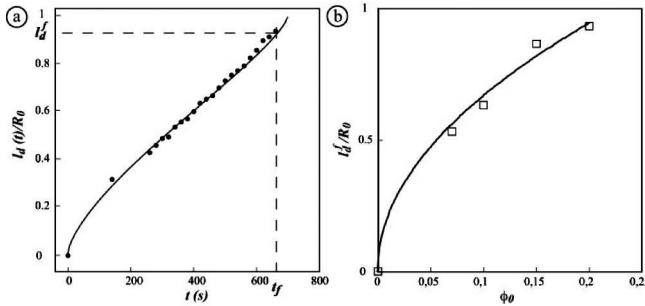


Fig. 3. (a) Time variations of the width l_d of the gelled foot to the initial radius R_0 of the sessile drop. Measurements (dots) are well fitted by eq. (2) (line). (b) Final width l_d^f of the gelled foot to the radius R_0 as a function of the initial volume fraction ϕ_0 ; line is a square root power.

temperature). Equation (1) is usually valid for colloidal dispersions as long as the liquid/air menisci stay at the surface of the drop. Moreover the lifetime of a sessile drop is quantitatively described by the drying time t_D defined as $t_D = \frac{R_0}{V_E}$. Physically, this timescale corresponds to the complete drying time of a pure water sessile droplet of contact base radius R_0 .

As soon as evaporation begins, particles accumulate near the three-phase line: this contact line is strongly pinned on the substrate. As a result, a gelled foot forms at the drop periphery. It progressively extends while the fluid part regularly shrinks [1] (fig. 1b). Using mass conservation and assuming a wedge shape for the foot, the width l_d of the deposit, at time t , can be estimated as [2]

$$\frac{l_d(t)}{R_0} = \sqrt{\frac{\phi_0}{4\phi_g}} [1 - (1 - t/t_f)^{3/4}]^{2/3}, \quad (2)$$

where ϕ_g is the packing fraction in the deposit and t_f is the elapsed time before the gelled foot ceases to grow. Initially there is no ring, and at time t_f the foot contains all the non-volatile solutes. Measurements of the foot extent with time are well fitted by eq. (2) as shown in fig. 3a. This foot exhibits a final width l_d^f that approximately increases with the square root of the initial particles volume fraction, ϕ_0 , in accordance with eq. (2) (fig. 3b).

3.2 Channeling cracks formation

3.2.1 Elapsed time for crack formation

During the gelled foot extent, large drying stresses build up as a result of pressure gradient in the pore liquid. Since the film is free to contract vertically in response to stress, the shrinkage at the free surface is frustrated by the adhesion on the substrate. The threshold value is correlated with the maximum pressure that can be supported by an array of particles, that is the capillary pressure $P_{cap} \propto -\frac{\gamma_{w,a}}{r_p} \sim -10^7$ Pa, where r_p is the pore radius, close to the particle radius a .

At time t_c , a first crack nucleates from the three-phase line and propagates along a radial path in the gelled foot (first image in fig. 4). A simple view of the gelled foot points out why the crack propagates along a radial path. In this way, let us compare the components of the mechanical stress field in an idealized thin ring of constant thickness h (fig. 1c). The equilibrium of the corresponding internal forces in a thin ring implies $\frac{\sigma_{\theta\theta}}{\sigma_{rr}} \sim \frac{r}{l_d} \gg 1$ with σ_{rr} and $\sigma_{\theta\theta}$, respectively, the radial and ortho-radial components of the stress field in cylindrical coordinates. Thus the main component of the stress in the ring is the ortho-radial one. As a result the crack path is radial, and is aligned perpendicular to the retreating solidification front.

The time t_c , that is elapsed before cracks propagate in the gel, appears to be a well-defined quantity as shown by the statistic in the inset of fig. 5(a); these measurements are performed on drying drops under given drying conditions (RH, T) and for similar sessile drops (R_0, θ_0). In addition the mean elapsed time for crack formation appears to be dependent on the mechanical properties of the gel. In particular, experimental results show that this elapsed time is longer for gels exhibiting lower elastic modulus (fig. 5).

Once the first crack forms in the gelled foot, a pattern of radial cracks build up all around the drop edge during a duration Δt . Figure 4 shows a typical sequence of cracks formation during the drying process of a sessile drop in room conditions. The resulting pattern exhibits well-defined periodicity in space and in time.

3.2.2 Spatial periodicity

The well-defined crack spacing, λ , is reported as a function of the foot height e_c , defined in fig. 6 (inset). The quantity e_c depends on the contact angle of the drop on the substrate, and consequently is controlled by modifying its surface. Measurements highlight that the crack spacing, λ , linearly increases with the foot height, e_c , in the range of thickness studied [14]. Then, the array of radial cracks propagates during the gelled foot extent.

3.2.3 Temporal periodicity

The formation of cracks can be experimentally pointed out by the space-time diagram presented in fig. 7. Such a diagram is constructed by recorded successive radial crack formation with time. The horizontal axis stands for the angular position of a crack whereas time runs toward the bottom in the vertical axis. The constant slope in the diagram (red dashed line) suggests that the period δt between two consecutive cracks is approximately constant for given drying conditions.

Overall, the crack distribution reveals a complex stress field in the material. Since a single radial crack is not sufficient to release all the stress in the material, the spatial and temporal periodicity of the crack network strongly suggest that the mechanical stress continues to build up

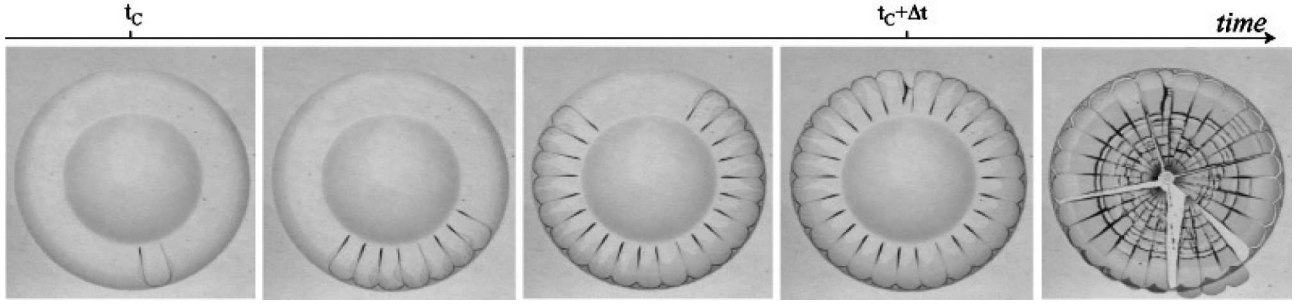


Fig. 4. Sequence of cracks formation during the drying process of a sessile drop of a silica dispersion (HS-40 dispersion, $\phi_0 = 0.20$; $\theta_0 = 30^\circ$; $2R_0 = 4$ mm; $RH = 50\%$): a regular pattern of radial cracks forms all around the gelled periphery, while the central part of the drop is still fluid; here $t_c = 15$ min and $\Delta t \sim 75$ s. Then cracks propagate as and when the solidification front limiting the gel phase from the liquid phase propagates toward the drop center. When the radial cracks reach the center of the drop, ortho-radial cracks connect to the radial crack pattern; finally de-adhesion can take place.

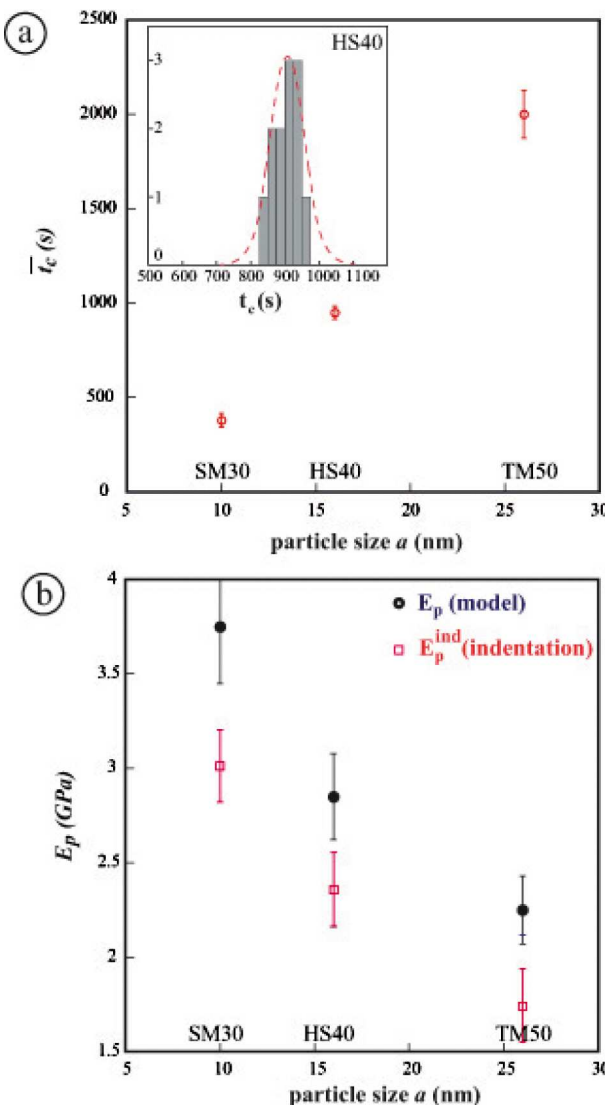


Fig. 5. (a) Elapsed time before the first crack forms for various silica gels. Inset: statistics on elapsed time for crack formation, t_c , for sessile drops of HS-40 dispersion. (b) Elastic modulus for various silica gels; E_p^{ind} is obtained using indentation testing at time t_f , and E_p is deduced from eq. (5).

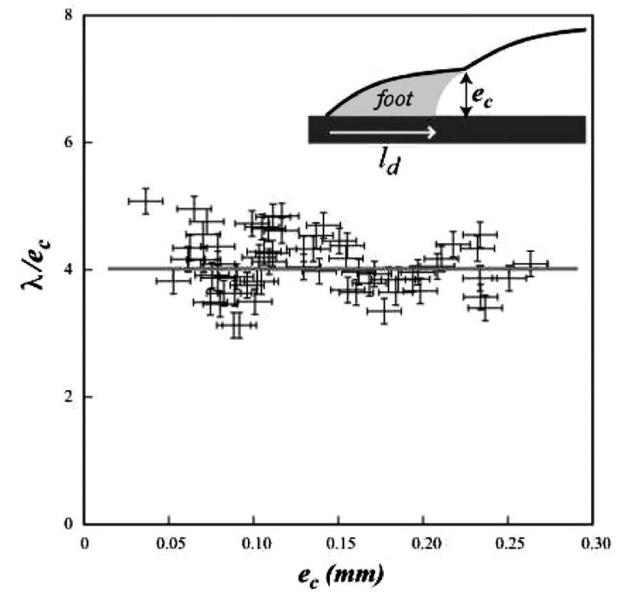


Fig. 6. Well-defined crack spacing. The crack spacing λ is plotted as a function of the maximum foot height e_c measured when cracks form (HS-40 dispersion, base diameter 4 mm and $RH = 50\%$). The straight line is the mean value of $\frac{\lambda}{e_c}$.

during the radial cracks formation. Such a dependence was approached by the coupling between stress relaxation and evaporation through new surfaces created when cracks appear [15].

3.2.4 Effect of the drying kinetics on the crack patterns

The spatial periodicity of the crack patterns, and the elapsed time for crack formation strongly depend on various physical parameters such as the physicochemical system [16], the substrate [17,18], and the drying conditions [19]. In particular the relative humidity of the surrounding air is one of the easiest parameters to be controlled. In this way, sessile drops exhibiting same initial liquid volume and contact angle were dried at different rel-

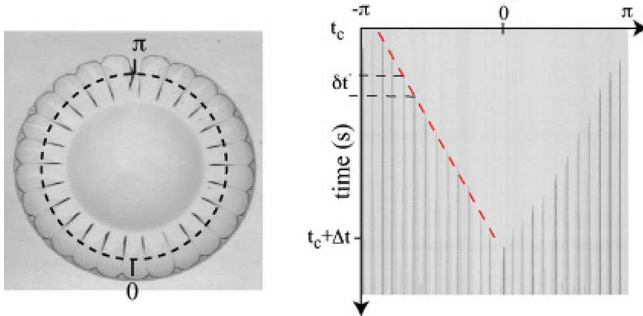


Fig. 7. Well-defined temporal periodicity. Left: image of a drop exhibiting radial crack pattern all around its periphery (HS-40 dispersion, base diameter 4 mm and $RH = 50\%$). When a radial crack forms, its intersection with the dashed circular line is recorded in time: it gives the period δt between two successive cracks. Right: resulting spatio-temporal diagram: each grey vertical line corresponds to the formation of a radial crack; the period between two consecutive cracks is $\delta t \sim 3$ s.

ative humidity RH ; as a result different crack patterns are displayed in fig. 8: the number of radial cracks distinctly decreases when the drying rate is lower. In addition, an increase of the relative humidity is accompanied by an increase of the width of the gelled foot at time cracks form: $l_d(t_c) \equiv l_d^c$. In particular, for high relative humidity ($RH > 90\%$), the whole drop is gelled before cracks form. Moreover, measurements of the elapsed time for crack formation are plotted as a function of the relative humidity in fig. 9: the elapsed time t_c appears to increase with the relative humidity.

Finally the effect of the drying rate on the crack pattern can be qualitatively investigated by drying two droplets that are placed on a substrate at distance from each other. Evaporation rate of droplets interferes strongly, affecting locally the crack patterns and the final shape of the deposits left (fig. 10) [20].

3.2.5 Discussion

The elapsed time for crack formation increases when the gel elastic modulus is lower (fig. 5). A simple model, based on the drying stress build-up, suggests this current.

In the gel phase, the spatial variation in pore pressure can be estimated using the theory of poro-elasticity [21]; this theory is based on linear constitutive relations coupled with Darcy law for fluid flow in the porous medium. At a fixed distance r from the drop center, the local thickness of the gelled foot is $h(r) \equiv h_r$, and the local liquid pressure p in the pores obeys a one-dimensional diffusion equation along the z vertical direction

$$\frac{\partial p}{\partial t} = D_p \frac{\partial^2 p}{\partial z^2}, \quad (3)$$

where $D_p = \frac{k E_p}{\eta_0}$ is the diffusivity, or consolidation coefficient, with E_p the elastic modulus of the gel (assumed to be constant), and η_0 the viscosity of the solvent flowing

Table 2. Elastic moduli E_p^{ind} of HS-40 gels dried for three relative humidities RH . Measurements are performed by indentation testing at time t_f .

| RH ($\pm 2\%$) | E_p^{ind} (± 0.4 GPa) |
|-----------------------|--|
| 20 | 4.2 |
| 40 | 2.8 |
| 86 | 1.5 |

through the porous gel of permeability k . For randomly packed monodispersed spheres k is given by the Carman-Kozeny relation: $k = \frac{1}{45} \frac{(1-\phi_g)^3}{\phi_g^2} a^2$, where ϕ_g is the particle volume fraction of the gel phase ($\phi_g \sim 0.6$) and $k = 2.3 \times 10^{-19} \text{ m}^2$. For film thicknesses ranging between 100 and 500 μm , a typical rigidity of the porous network is measured just after cracks formation ($E_p = 1 \text{ GPa}$ [22]). Moreover a steady rate of evaporation V_E is assumed at the upper surface of the gel $z = h_r$: the Darcy law gives the gradient of liquid pressure at the upper surface of the gel

$$\frac{\partial p}{\partial z} |_{z=h_r} = - \frac{V_E \eta_0}{k}. \quad (4)$$

Equation (3) together with the boundary condition (4) give the pore pressure distribution $p(z, t)$ [9]. Indeed, considering the gel initially uniform without pressure gradient ($p(z, t=0) = p_0$), the stress in the plane of the film expresses as: $\sigma(z, t) \propto p_0 - p(z, t)$. In particular, eqs. (3) and (4) show that the pore pressure linearly increases with time. At the upper surface of the film the drying stress simply expresses as $\sigma(h_r, t) \approx E_p \frac{t V_E}{h_r}$. When the drying stress exceeds a threshold value, says at time t_c , it is released by the formation of cracks.

We assume that cracks form as soon as the liquid pressure in the pore is close to P_{cap} , that is as soon as the drying stress reaches a value close to $-P_{\text{cap}}$: $\sigma(h_r, t_c) \approx -P_{\text{cap}}$. As a result eqs. (3) and (4) allow us to express t_c as

$$t_c \approx \frac{(-P_{\text{cap}})}{E_p} \frac{h}{V_E}, \quad (5)$$

where h is a typical thickness of the gel, assumed to equal the foot height e_c in the following.

Thus, estimating t_c , eq. (5) gives an order of magnitude of the elastic modulus of the gel phase at the cracking onset. In this way values of the elastic modulus, E_p , deduced from eq. (5) are shown in table 1, for three silica gels at $RH \sim 50\%$. These estimations are in good agreement with measurements using indentation testing, E_p^{ind} , despite of the inaccuracy (fig. 5b).

In addition, the elastic moduli E_p^{ind} of dried gels dried are reported in table 2 for different drying conditions, *e.g.* RH . These measurements were obtained using indentation testing. Putting the value of E_p^{ind} in eq. (5) allows us to highlight that the elapsed time for crack formation increases with the relative humidity of the surrounding air (fig. 9).

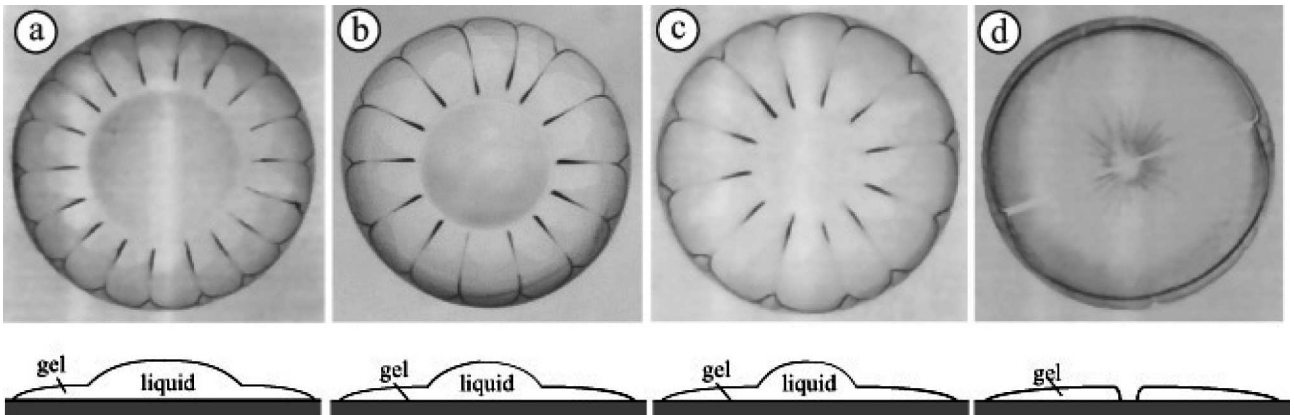


Fig. 8. Crack patterns in different colloidal sessile drops as a function of the drying conditions, e.g., RH . Images in top view were taken just after cracks formation, and corresponding sketches in side view (HS-40 dispersion, initial contact angles are 40° and each drop base diameter is 3 mm). RH : (a) 20%; (b) 40%; (c) 60%; (d) $> 90\%$ (in the last case, cracks are formed when the whole drop is gelled).

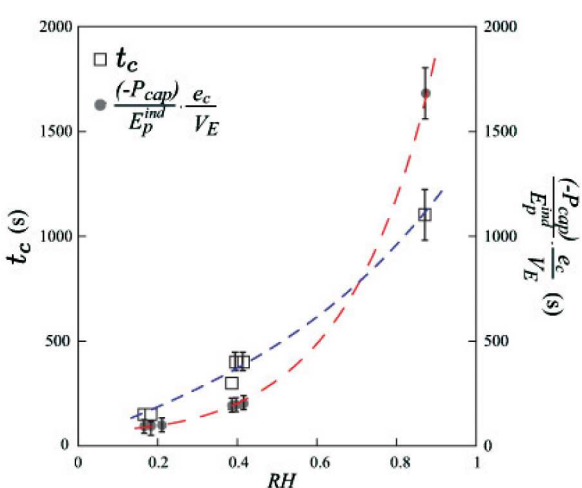


Fig. 9. Left axis: measurements of the elapsed time for crack formation t_c as a function of the relative humidity RH . Right axis: the quantity $(-P_{cap}) / (E_p^{ind} \cdot e_c / V_E)$ is plotted as a function of the relative humidity RH ; $P_{cap} \sim -10^7$ Pa, E_p^{ind} is the elastic modulus of the gel phase measured using indentation testing at time t_f (table 2).

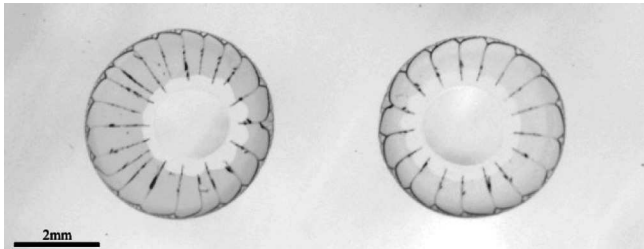


Fig. 10. Interaction of two identical drying droplets that are placed on a substrate at distance from each other; silica dispersion Ludox HS-40 dried at room temperature and $RH \sim 40\%$.

Finally, the influence of the drying rate on the crack patterns suggests that the mechanical properties of the gel are strongly affected by the drying kinetics (fig. 8). This suggests that the internal structure is probably modified by the consolidation kinetics, also the organization of the particles in the gel that is formed [23].

4 Conclusion

In this paper, we have studied some mechanical instabilities induced by the drying process of sessile drops of concentrated silica dispersions. In particular, the formation of cracks exhibits a well-defined spatial pattern spatially and temporally. These results appear to be generic in drying drop of silica sols, and can also be observed in drying drops of colloidal dispersions of rigid latex particles. Moreover, it appears that the features of the crack morphologies provide information on the mechanical properties of the system and the way it is consolidated. Indeed, the onset of cracking occurs after a well-defined elapsed time that depends on the mechanical properties of the gel, and on the drying kinetics. The estimation of the elapsed time for crack formation is related to the elastic properties of the material. This is supported by quantitative measurements using indentation testing, and by a simple scaling law derived from poro-elastic theory. However this simple model does not allow us to explain the well-defined periodicity in space, and in time of the crack pattern, but only highlight the stress build-up all along the crack pattern formation.

We are grateful to the late C. Allain.

References

1. F. Parisse, C. Allain, Langmuir **13**, 3598 (1997).
2. R.D. Deegan, Phys. Rev. E **61**, 475 (2000).
3. L. Pauchard, B. Abou, K. Sekimoto, Langmuir **25**, 6672 (2009).
4. L. Pauchard, V. Lazarus, B. Abou, K. Sekimoto, G. Aitken, C. Lahanier, Reflets Phys., Soc. Franç. Phys. **3**, 5 (2007).
5. D. Brutin, B. Sobac, B. Loquet, J. Sampol, J. Fluid Mech. **667**, 85 (2011).
6. D. Brutin, B. Sobac, C. Nicloux, J. Heat Transfer **134**, 061101 (2012).
7. B. Derjaguin, L. Landau, Acta Physicochim. URSS **14**, 633 (1941).
8. E.J. Verwey, J.T.G. Overbeek, *Theory of Stability of Lyophilic Colloids* (Elsevier, Amsterdam, 1948).
9. C. Brinker, G. Scherer, *Sol-Gel Science: The Physics and Chemistry of Sol-Gel Processing* (Academic Press, New York, 1990).
10. H. Bergna, *The Colloid Chemistry of Silica* (American Chemical Society, 1994).
11. W. Oliver, G. Pharr, J. Mater. Res. **7**, 1564 (1992).
12. L. Pauchard, C. Allain, Europhys. Lett. **62**, 897 (2003).
13. H.S. Carslaw, J.C. Jaeger, *Conduction of Heat in Solids* (Oxford University Press, London, 1959).
14. C. Allain, F. Parisse, L. Limat, Bull. S. F. P. **103**, 24 (1996).
15. C. Allain, L. Limat, Phys. Rev. Lett. **74**, 2981 (1995).
16. L. Pauchard, F. Parisse, C. Allain, Phys. Rev. E **59**, 3737 (1999).
17. A. Groisman, E. Kaplan, Europhys. Lett. **25**, 415 (1994).
18. M.I. Smith, J.S. Sharp, Langmuir **27**, 8009 (2011).
19. B.D. Caddock, D. Hull, J. Mater. Sci. **37**, 825 (2002).
20. M. Kobayashi, M. Makino, T. Okuzono, M. Doi, J. Phys. Soc. Jpn. **79**, 044802 (2010).
21. M.A. Biot, J. Appl. Phys. **12**, 155 (1941).
22. F. Boulogne, L. Pauchard, F. Giorgiutti-Dauphiné, Soft Matter **8**, 8505 (2012).
23. G. Gauthier, V. Lazarus, L. Pauchard, EPL **89**, 26002 (2010).